Article:
Azam, A orcid.org/0000-0002-3510-1333, Dorgham, A, Khaemba, DN et al. (3 more authors) (2020) Understanding the role of surface textures in improving the performance of boundary additives, part II: Numerical simulations. Tribology International, 152. 106252. ISSN 0301-679X

https://doi.org/10.1016/j.triboint.2020.106252

Understanding the role of surface textures in improving the performance of boundary additives, Part II: Numerical simulations

Abdullah Azam[1], Abdel Dorgham[1], Doris Nekesa Khaemba[2], Farnaz Motamen Salehi[1], TianLong See[2], Anne Neville[1]

[1] *Institute of Functional Surfaces (IFS), University of Leeds, LS2 9JT*
[2] *The Manufacturing Technology Centre, CV7 9JU, Coventry UK*

Abstract

Tribological performance of mating surfaces can be improved by developing surfaces with predefined textures and it is crucial to understand their role in modifying the performance and action of boundary lubrication additives. An isotropic texture T1, intermediate texture T2 and anisotropic texture, T3, were imported into our mixed simulation framework. It was found that T3 outperforms by providing the most feasible conditions for the activation of the lubricant additive, molybdenum dithiocarbamate (MoDTC) i.e. generating higher pressure peaks (shear), making more lubricant (reactant) available and providing greater load bearing area (greater reaction probability). Hence, facilitating the formation of functional boundary films. T2 seems to generate highest pressure peaks but its performance is worst due to its inability to sustain lubricant within the contact.

Keywords: `mixed lubrication, tribofilm, friction`,

1. Introduction

Reduction of friction and wear is generally achieved by introducing a lubricant between the contacting surfaces. For low to moderate pressure cases, the lubricant successfully protects the surfaces. If the contact severity increases, the lubricant film breaks and the lubricant rheology is not sufficient to reduce friction and wear. Therefore, certain additives are added into the lubricants to address various issues under different lubricating conditions. The most important lubricant additives are antiwear (AW) and friction modifier (FM) additives. These additives interact with each other and with the contacting surfaces to form functional films and the rate of formation of these films rapidly increases when mechanical energy is available within the

contact. Therefore, these films are also called tribofilms [1], owing to their tribo-chemical formation route. The interaction of these additives with the surface texture and roughness is complex and unclear. Due the growing use of textured surfaces to improve and control contact performance, it is getting increasingly important to understand the interaction of these lubricant additives with the surface features.

The ability to tune the tribological contact performance by using surface textures has a key advantage that the original system and operating parameters can be kept unchanged. Therefore, surface textures are a cheaper and simpler alternative to control friction at the tribological interface as it avoids component redesign and are easy to utilize in existing and future technologies [2].However, the manufacturing and fabrication of textured surfaces incurs additional costs, requiring justification over the benefits obtained [3].

Surface textures were explored for controlling friction first in 1960s [4] and were successfully used in reducing friction at the piston ring-liner contacts as early as 1949 [5] but the challenges associated with the predicting and understanding the effect of friction in textured surfaces still hinders their widespread use [2]. Friction is a complex phenomenon and is affected by several parameters of the tribo-system. The most important parameter being the surface roughness. For simple systems, there have been several attempts to control or reduce friction through proper texturing techniques but for systems where chemical interactions between the surface and lubricant additive start to dominate the overall operation, these simple techniques fail to provide adequate means to understand and control friction. The complications arise because the action of the boundary lubrication additives is considered to be due to shear at the interface [6] and this shearing force is modified by the presence of these surface textures.

The ability to create surface features with great precision and repeatability has opened up new avenues to the use of surface texturing in contacts. Some of the key application areas include cutting tools, metal forming tools, mechanical sealing and piston-cylinder liners [7–10]. The technique of surface texturing is based upon producing simple geometrical features like grooves and chevrons [11] with certain arrangement of these features on the surfaces by controlling the distance and layout and the geometrical size of these simpler features. It is postulated, and has been seen in many applications as well, that the presence of these features on the surface can improve the friction and wear performance within the contact. Several mechanisms have been proposed like the increased lubricant film thickness, reduction in the real contact area and the possibility of entrapment of the wear debris in these features [12].

It is evident that the same texture may not perform well under all lubrica-

tion conditions but it is the ultimate goal to find textures that can work with additive containing and additive free systems and across lubrication regimes. Several mechanisms have been related to the improved performance of surfaces with textures. A large number of studies have been done in the past to understand the key mechanisms of performance of surface textures. A group of researchers believe that it is the ability of surface textures to increase the load support that gives these surfaces superior performance and result in reduced friction [13–22]. On the other hand, some researchers believe that the textured surfaces outperform non-textured surfaces by providing a debris trapping mechanism where the wear debris gets trapped in the texture features and thereby smoothing the overall surface, resulting in reduced friction and wear [15, 23–26]. In addition, there are a number of studies suggesting that the textured surfaces can entrap lubricant within the texture patterns and provide a contingency supply of lubricant to ensure friction and damage remains minimum [15, 23, 27–30]. Moreover, it has been suggested that the surface texture can halve the static friction compared to non-textured surfaces if optimum texture geometry is used [31].

The surface texture does not always provide benefits. Vladescu et al. [32–37] have recently published a series of papers suggesting that the positive or negative effect of surface texture depends upon the lubrication regime it experiences in operation. They found that under boundary and mixed lubrication conditions, the film thickness increases and friction reduces while the same texture performs the opposite under EHL and hydrodynamic lubrication conditions [35]. They also observed that the lubricant film thickness increases due to individual lubricant pockets and found that these small film thickness transients can cause significant reduction in the friction values owing to the steepness of the Stribeck curve (especially in the mixed lubrication regime) and the combined effect of the contribution of these individual lubricant pockets [34]. They also showed that under extreme conditions of highly loaded contacts, surface texturing provides lubricant replenishment and reduces wear [36].

The experimental results obtained in the authors' complimenting article [38] showed that certain textures outperform others but the reasons behind these were unknown. This was mainly due to the difficulties in performing experiments under the boundary and mixed lubrication conditions [3, 39]and the inability of experiments in providing detailed pressure and film thickness information. Therefore, the current study aims at understanding and unfolding the effects of surface textures on the boundary additives by using lubrication simulations. The experimental texture values were used as input in the in-house mixed lubrication codes to enable the simulation of textured surfaces and to ensure the simulations are in line with experiments. The

mixed lubrication solvers have been well tested as evidenced in our previous modelling studies [40–43] and are being extended to even more complex experimental cases [44, 45]. The key parameters affecting the performance of these textures were identified and related to the experimental outcomes. The pressure and film thickness profiles from the textured surfaces were developed and compared against the non-textured sample results. An understanding of the effects of surface textures on boundary lubrication additives is developed by analyzing the contact and lubrication parameters.

The paper is arranged by first presenting the details of the lubrication model. The model is capable of simulating the entire transition from full film to boundary and dry lubrication conditions. Next, the numerical solution details are presented followed by the results and discussion section. Finally, the conclusion section closes the paper.

2. EHL / Mixed Lubrication Solver

The lubrication model used in this current study can simulate the entire lubrication transition from full film to elastohydrodynamic lubrication (EHL) to mixed lubrication down to boundary lubrication conditions. The numerical solver contains five equations (described below). These equations together form a complete set that can be solved using numerical discretization to get the system of equations which can be solved by using appropriate linear algebra techniques. To enable the model to handle the mixed contact conditions and extreme conditions of low speed and high load, the contribution from the entrainment flow terms is also considered while building the coefficient matrix to ensure diagonal dominance and numerical stability under all lubrication conditions. Moreover, certain advanced concepts like the semi-system approach [46] and unified solution algorithm [47] are implemented into the framework. This enables the solution in a unified manner where both the lubricant and solid contact pressures are calculated by solving the Reynolds equation coupled with deformation. A flow chart is provided for clarity and understanding of the lubrication solution algorithm in figure 1. The equation system defining the mixed lubrication solver are presented below.

The complete pressure profile is computed by solving the Reynolds equation, given as

$$\frac{\partial}{\partial x}\left[\left(\frac{\rho h^3}{12\eta}\right)\frac{\partial p}{\partial x}\right]+\frac{\partial}{\partial y}\left[\left(\frac{\rho h^3}{12\eta}\right)\frac{\partial p}{\partial y}\right]=\left(\frac{u_1+u_2}{2}\right)\frac{\partial(\rho h)}{\partial x}+\frac{\partial(\rho h)}{\partial t} \quad (1)$$

The variables h, ρ and η define the lubricant film thickness, density and viscosity. The pressure, speed of body 1 and speed of body 2 are given by p,

u_1, u_2 while x, y represent the coordinate directions and t is the time. The lubricant properties are described through its viscosity. In this study the lubricant is assumed to be Newtonian and the x-coordinate is aligned with the flow direction. Two boundary conditions are applied. At the boundaries of the solution domain, the boundary condition $p = 0$ is applied. The exit of the EHL contact is diverging and the pressure in this region may fall below the vapour pressure and results in fluid cavitation [48]. The boundary condition to handle this phenomenon is called Swift-Steiber boundary condition or the Reynolds exit conditions and enforces the pressure beyond cavitation boundary, x_e, to be zero i.e. $\{\forall\ x \geq x_e,\ p < 0 \Rightarrow p = 0\}$.

The film thickness equation for the point contact is expressed by combining all the terms defining the gap between two surfaces.

$$h = h_0(t) + \frac{x^2}{2R_x} + \frac{x^2}{2R_y} + v_e(x, y, t) + \delta(x, y, t) \tag{2}$$

The film thickness is also termed as gap as it defines the relative gap between mating surfaces. In this equation, $h_0(t)$ is the undeformed film thickness. The term v_e describes the total deformation. The deformation may be elastic or elasto-plastic. At this stage the deformation cannot be separated into individual components. The algorithm presented in the next section outlines the procedure for extracting the magnitude of plastic deformation. The variables R_x and R_y define the radius of curvature in the x and y direction respectively while the term $\frac{x^2}{2R_x} + \frac{x^2}{2R_y}$ gives the macro geometry of the contact. The microgeometry is defined deterministically by the roughness term $\delta(x, y, t)$. The surface elastic deformation v_e is represented by the famous Boussinesq integral formulation.

$$v_e(x, y) = \frac{2}{\pi E'} \int\int_{\sigma} \frac{p(x', y')}{\sqrt{(x - x')^2 + (y - y')^2}} dx' dy'$$

where $v_e(x, y)$ is the deformation at point (x, y) due to pressure at point (x', y').This equation is non-dimensionalised and converted into discrete form and represented as a deformation matrix.

$$V_{ij} = 2\frac{\Delta X}{\pi^2} \sum_{k=1}^{M} \sum_{l=1}^{N} D_{ij}^{kl} P_{kl}$$

In this equation, the matrix D_{ij}^{kl} is called the flexibility matrix and the pressure $P_{kl} = p_{kl}/P_h$, where P_h is the Hertzian pressure. This matrix forms a convolution with pressure which can be solved more efficiently using Fast Fourier Transforms (FFTs). The use of FFTs makes the solution process

much quicker and makes denser grids accessible. The deformation matrix is written as a convolution.

$$V(X_i, Y_j) = \sum_{k=1}^{M-1} K(X_i - X_k, Y_j - Y_k) * P(X_k, Y_k)$$

The application of FFTs require the conversion of this linear convolution to a cyclic convolution and the pressure matrix and the flexibility matrix require pre-treatment [49]. The Direct Convolution (DC) FFT method is computationally much more efficient compared to the other methods for calculation of surface deformation [50]. The viscosity is considered a function of pressure and the Roelands equation is used to describe it.

$$\eta(p) = \exp\left(\ln(\eta_0) + 9.67\right)(-1 + (1 + \frac{P_h}{p_0}p)^z) \tag{3}$$

The term η_0 is the viscosity at ambient conditions and z is a dimensionless parameter called Roelands pressure viscosity index obtained through curve fitting. In the current study, z=0.68 was used. The lubricant density is also considered a function of pressure and is calculated using the following equation,

$$\rho = \rho_0 \left(1 + \frac{0.6 \times 10^{-9} p}{1 + 1.7 \times 10^{-9} p}\right) \tag{4}$$

The load balance equation ensures that the applied load is balanced by the resulting pressures and is given in dimensional form, for a point contact as,

$$\sum_{x_i, y_i}^{x_o, y_o} p(x, y) dx dy = W \tag{5}$$

where the i and o values correspond to the inlet and outlet of the solution domain, respectively and W represents the applied load.

3. Numerical details

The five equations (1 to 5) form a complete set which is solved to get the mixed lubrication pressure and film thickness profiles. These Reynolds equation is discretized using finite differencing. In equation 1, the two terms on the left-hand side are discretized using the central difference scheme and the two terms on the right-hand side are discretized using the backward difference scheme. The solution to the discretized Reynolds equation yields contact pressures which are used to update the deformation, film thickness, viscosity, density and finally, the Reynolds coefficients. These coefficients are

then used to estimate pressures again. An iterative solution process is applied to calculate pressures at each step until convergence. The convergence is established by ensuring that the relative pressure difference $\frac{\sum(P^{new}-P^{old})}{\sum P^{old}} \leq 1\times10^{-5}$ in each iteration. The convergence of load balance is applied through the undeformed gap, $h_0(t)$ in equation 2. The load balance convergence is also applied by ensuring that, for a single time step, the relative difference, $\frac{h_0^{new}-h_0^{old}}{h_0^{old}} \leq 1\times10^{-4}$. The solution procedure is designed to ensure that more information is available at the current iteration step.

Two numerical grid sizes were used to see the relative difference in the imported texture information. For the mesh justification, in the current study, the difference in the film thickness was found to be less than 1 % when the mesh density was changed from 128 × 128 to 256 × 256. To be consistent with the experimental grid size, a numerical grid of 256 × 256 was used. This corresponds to a numerical grid size of 1.9 μm which is close to the experimental grid size of 1.4 μm. The input conditions were similar to those used in the experimental work and are given in table 1.

4. Results and Discussion

The surface texture information was directly imported from the experimental measurements alongwith the non-textured sample roughness information. This was done to ensure that the exact textured data is given as input to the simulation models. The imported texture and roughness information is shown in figure 2 with the x and y axis representing the 256 × 256 numerical grid size. Selected geometrical parameters for these textured and the non-textured surfaces are presented in table 2. These textures have similar R.M.S. roughness values and all have negative skewness, indicating that most of the material is above the mean line. These textured surfaces can be identified through the texture direction, S_{td} and the texture aspect ratio S_{tr}. From table 2, it can be seen that the S_{td} value for both T1 and T3 is 90^o and for T2 and the non-textured sample, it is 60^o and 133^o, respectively. For the non-textured sample, the texture direction is not considered important, owing to its significantly lower R.M.S. roughness. But, due to the fact that both T1 and T3 have the same texture direction, the texture direction, the differences in sliding direction for each of these textures makes their behaviour different within the contact. The S_{tr} value for T1 is close to 1 indicating a nearly isotropic surface. This is because of the laser scanning paths used to achieve the pattern. On the other hand, S_{tr} for T3 was close to 0 indicating an anisotropic surface due to the fact that a single-direction laser scanning path was employed in processing T3. Therefore, the results presented in

this section have a direct correlation with the micro-texturing patterns and processes used to create the surfaces opening up infinite possibilities for developing surfaces to fine tune the required tribological performance.

The comparison of different textured surfaces is performed by comparing their tribological performance. The key parameters used are the lubricant film thickness, lambda ratio, contact area ratio and the contact load ratio. The lubricant film thickness is presented as the average film thickness, obtained by averaging the film thickness values in $\frac{2}{3}rd$ of the Hertzian zone. The lambda ratio is the ratio of the average film thickness to the composite roughness of both the surfaces. The contact area ratio defines the percentage of area under dry / boundary lubricated conditions. This parameter is directly linked to friction and is also a factor in determining the probability of tribochemical reactions as these are dependent upon the activated area and the greater the activated area (area with higher shear), the greater is the probability of reaction. The contact load ratio defines the percentage of load carried by the dry contact regions within the Hertzian contact zone. This ratio is directly related to the amount of shear energy present within the contact and as experimentally observed [6], the formation of tribofilms is a shear based process.

First of all, the lubrication regime was explored by varying the speed. It is expected that the textures with the ability to hold thicker lubricant films will be able to provide conditions more suited to the dissociation of boundary lubricant additives and the acceleration of the formation of functional films. This statement is only complete if the textures with thicker films are also able to sustain more shear. Therefore, textures with an optimal combination of lubricant film thickness and shear will be expected to perform the best.

In figure 3 the changes occurring in the average central film thickness as the speed changes from a very high value (10 m/s) to a very small value (0.0005 m/s) are shown. The plot resembles a sigmoid curve similar to the Stribeck curve. To develop these plots, the composite roughness of these surfaces was fixed ($R_q \approx 250nm$), keeping the surface texture features the same, and the sliding speed was varied to move from an EHL / mixed to pure boundary lubrication regime. The basic idea is to understand the lubrication transition behaviour of these textures. It can be seen from figure 3 that T3 and T2 can sustain more lubricant within the contact, even at lower speeds. At speeds greater than 0.2 m/s, texture 3 has the thickest lubricant films entrapped while the non-textured surface and T2 have the thinnest lubricant films entrapped. T1 and T3 have similar lubricant film thickness values at speeds lower than about 0.2 m/s.

Next, the lambda ratio values are presented in figure 4. The lambda ratio values represent the severity of the contact configuration. In simulations, the

exact speed at which the dry contact patches start to appear within the Hertzian contact zone can be identified. Therefore, the speeds corresponding to the dashed lines in figure 4 represent the state when the dry contact patches appear first within the contact. The dashed lines have been color coded to the solid line for the corresponding texture. It should be noted that with decreasing speed, the quantity of these contact patches increases. It can be seen that for all speeds, T1 and T3 have the highest value of lambda ration suggesting that these textures feel the least severity during the speed transition. For T2 and the non-textured sample, the lambda ratio values are very similar but the dashed lines show that the transition from EHL to mixed starts at a speed of ≈ 3 m/s for T2 while for the non-textured sample, the transition starts at a speed of 0.2 m/s. The transition from EHL to mixed starts at similar speeds (≈ 0.2 m/s) for both, T1 and T3. At slightly higher speeds, ≈ 1.1 m/s, a crossover point can be seen where the lambda ratio values for both T1 and T3 cross each other. A close look at both figure 3 and figure 4 shows that T2 and the non-textured sample will have more shear within the contact compared to T1 and T3 due to very severe values of lambda ratio. But due to the fact that T3 and T1 have thicker lubricant films entrapped, at the corresponding lambda ratio or speed. This ensures that more lubricant is present to enable the tribochemical reaction between the substrate and boundary lubrication additives, unlike the non-textured and T1 samples. Therefore, the simulation results, at this stage support our experimental results, indicating superior performance of texture 3 for additive dissociation and tribofilm formation.

Another parameter that has direct consequences for the additive action is the real area of contact, A_c and the contact load ratio W_c. The W_c can be directly linked to the shear at the interface while the parameter A_c can be linked to the probability of tribofilm formation (more local contacts lead to more tribofilm formation). The greater the W_c and A_c, the greater the chances of additive decomposition and tribofilm formation. These parameters are plotted in figure 5. It can be seen that the contact load carried by the dry contact part within the Hertzian contact zone is zero for all the textured surfaces until the speed falls below 10 m/s. In numerical simulations, it is generally assumed that as the contact load reaches 80 %, the contact can be considered to be in pure boundary. This assumption is valid as the contact characteristics under such circumstances is governed, mainly by the dry contact regions. In figure 5, this has been marked by the dashed line at 80 % contact load ratio. Accordingly, at the lowest speeds of 0.0005 m/s, both texture 2 and the non-textured sample have already reached boundary lubrication status. In fact, T2 achieves boundary lubrication at speeds as low as 0.02 m/s while the non-textured sample reaches full boundary lubrication

at speed very close to 0.001 m/s. On the other hand both T3 and T1 are still in the mixed state even at the lowest speed. It can be seen that throughout the speed range, under mixed lubrication state, W_c is always greater for T3 indicating more shear compared to T1.

The behaviour of contact area ratio with speed is evidently different as shown in figure 5. For the non-textured sample both A_c and W_c follow the same trend but for textured surfaces the trends are different. The A_c and W_c increase from 0 % at a speed of $\approx$ 0.3 m/s for both T1 and T3. Also, the increase in A_c and W_c follow similar trends for both these textures and with decreasing speed, the increase in A_c and W_c is at a similar pace. This behaviour is not observed in case of T2 where W_c is considerably greater than A_c for a given speed and achieves final values of $A_c \approx 65\%$, $W_c \approx 90\%$.

At first it may seem that T3 and T1 would be expected to have the least performance due to lower shear compared to the non-textured and T2 sample. However, it should be considered that lubricant shear can also cause additive dissociation and form tribofilms [6]. Taking this into account, T3 is still expected to perform better due to the availability of the adequate reactant to promote the formation of tribofilms and due to the availability of shear within the lubricant films. On the other hand, texture, T2 may have more shear at the interface within the dry contact patches but due to the absence of lubricant, this shear only goes into increasing friction and the temperature within the contact while no tribofilm can form. In order to understand the presence and role of shear, the pressures generated within the contacts with these textures were investigated.

The pressure profiles for all the textured surfaces are shown in figure 6 along with the pressure profile for the non-textured sample. It can be seen that all the textured samples produce significant pressure peaks but the highest pressure peak is generated by T3. The pressure profiles for T1 and T3 resemble in shape and periodicity but the magnitude of pressures generated in T1 is small. Moreover, T2 generates significant pressure disturbances throughout the contact region indicating presence of high shear. To illustrate the role of reactant in the dissociation of the boundary lubrication additives, film thickness profiles are presented in figure 7. The film thickness profiles clearly show that T2 has almost zero film thickness through most of the contact zone whereas T3 sustains the most lubricant within the contact. A comparison of film thickness profiles for T1 and T3 shows that T1 also holds significant lubricant within the contact but T3 holds a much thicker lubricant film. The non-textured sample has a zero lubricant film thickness value throughout the Hertzian contact zone.

In summary, the design of surface textues is highly application dependent and requires precise evaluation of individual application for developing a so-

lution for a tribo-system. A single optimum surface texture for all lubrication regimes is not possible [3]. Complexity arises due to the very large number of variables associated with the design of textured surfaces which is time consuming and expensive. Thus, "hit and trial" procedures are still a norm [51]. Another complexity arises due to the inherent nature of tribological systems that experience multiple lubrication regimes during single operation cycle. Moreover, the limitations of different surface texture fabrication techniques further complicates the system [52]. Therefore, it is immensely important to predict optimized surface texture parameters that are problem specific. In this study an effort was made to link the design of surface textures to tribochemically active systems.

5. Conclusions

In the current study, lubrication studies were performed on experimental surface textures to understand the role of surface textures in improving the dissociation of boundary lubrication additives. The experimental textures were imported into the in house mixed lubrication solver and the R_q value was fixed and the sliding speed (rolling speed) was changed from 20 (10) m/s down to 0.001 (0.0005) m/s. Texture 3 was found to provide the most feasible conditions for additive decomposition among all the textures by providing high pressure (shear) values combined with thicker lubricant films (reactants). Texture, T1 was found to have shear characteristics similar to T3 but its inability to retain thicker lubricant films and lower (in contact) pressures generation were found to be the key reasons for its inadequacy in supporting additive decomposition. Texture T2, on the other hand, provides the most shear and the pressure values are also high enough throughout the contact zone but the lubricant films within the contact are not thick enough to provide sufficient reactant. The non-textured sample was found to provide the least suitable conditions for additive decomposition and tribofilm formation.

References

[1] Hn Spikes. The history and mechanisms of zddp. *Tribology letters*, 17(3):469–489, 2004.

[2] FJ Profito, S-C Vladescu, T Reddyhoff, and D Dini. Experimental validation of a mixed-lubrication regime model for textured piston-ring-liner contacts. *Materials Performance and Characterization*, 6(2):112–129, 2017.

[3] C Gachot, A Rosenkranz, SM Hsu, and HL Costa. A critical assessment of surface texturing for friction and wear improvement. *Wear*, 372:21–41, 2017.

[4] James N Anno, JA Walowit, and CM Allen. Microasperity lubrication. 1968.

[5] LS Martz. Preliminary report of developments in interrupted surface finishes. *Proceedings of the Institution of Mechanical Engineers*, 161(1):1–9, 1949.

[6] J Zhang and H Spikes. On the mechanism of zddp antiwear film formation. *Tribology Letters*, 63(2):24, 2016.

[7] T Sugihara and T Enomoto. Performance of cutting tools with dimple textured surfaces: a comparative study of different texture patterns. *Precision Engineering*, 49:52–60, 2017.

[8] I Etsion and E Sher. Improving fuel efficiency with laser surface textured piston rings. *Tribology International*, 42(4):542–547, 2009.

[9] M Geiger, U Popp, and U Engel. Excimer laser micro texturing of cold forging tool surfaces-influence on tool life. *CIRP Annals*, 51(1):231–234, 2002.

[10] I Etsion and G Halperin. A laser surface textured hydrostatic mechanical seal. *Tribology Transactions*, 45(3):430–434, 2002.

[11] H Yu, X Wang, and F Zhou. Geometric shape effects of surface texture on the generation of hydrodynamic pressure between conformal contacting surfaces. *Tribology Letters*, 37(2):123–130, 2010.

[12] Z Wang, Y-B Li, F Bai, C-W Wang, and Q-Z Zhao. Angle-dependent lubricated tribological properties of stainless steel by femtosecond laser surface texturing. *Optics & Laser Technology*, 81:60–66, 2016.

[13] H Rahnejat, S Balakrishnan, PD King, and S Howell-Smith. In-cylinder friction reduction using a surface finish optimization technique. *Proceedings of the Institution of Mechanical Engineers, Part D: Journal of Automobile Engineering*, 220(9):1309–1318, 2006.

[14] A Kovalchenko, O Ajayi, A Erdemir, G Fenske, and I Etsion. The effect of laser surface texturing on transitions in lubrication regimes during unidirectional sliding contact. *Tribology International*, 38(3):219–225, 2005.

[15] A Borghi, E Gualtieri, D Marchetto, L Moretti, and S Valeri. Tribological effects of surface texturing on nitriding steel for high-performance engine applications. *Wear*, 265(7-8):1046–1051, 2008.

[16] D Braun, C Greiner, J Schneider, and P Gumbsch. Efficiency of laser surface texturing in the reduction of friction under mixed lubrication. *Tribology international*, 77:142–147, 2014.

[17] W Wang, Z Huang, D Shen, L Kong, and S Li. The effect of triangle-shaped surface textures on the performance of the lubricated point-contacts. *Journal of Tribology*, 135(2):021503, 2013.

[18] X Lu and MM Khonsari. An experimental investigation of dimple effect on the stribeck curve of journal bearings. *Tribology letters*, 27(2):169, 2007.

[19] AV Olver, MT Fowell, HA Spikes, and IG Pegg. inlet suction, a load support mechanism in non-convergent, pocketed, hydrodynamic bearings. *Proceedings of the institution of mechanical engineers, Part J: Journal of Engineering Tribology*, 220(2):105–108, 2006.

[20] M Fowell, AV Olver, AD Gosman, HA Spikes, and I Pegg. Entrainment and inlet suction: two mechanisms of hydrodynamic lubrication in textured bearings. *Journal of Tribology*, 129(2):336–347, 2007.

[21] M Scaraggi, F P Mezzapesa, G Carbone, A Ancona, and L Tricarico. Friction properties of lubricated laser-microtextured-surfaces: an experimental study from boundary-to hydrodynamic-lubrication. *Tribology Letters*, 49(1):117–125, 2013.

[22] H Bouassida, N Biboulet, P Sainsot, and AA Lubrecht. Piston ring load carrying capacity: Influence of cross-hatching parameters. *Proceedings of the Institution of Mechanical Engineers, Part J: Journal of Engineering Tribology*, 228(6):642–648, 2014.

[23] L Wang. Use of structured surfaces for friction and wear control on bearing surfaces. *Surface Topography: Metrology and Properties*, 2(4):043001, 2014.

[24] KH Zum Gahr, M Mathieu, and B Brylka. Friction control by surface engineering of ceramic sliding pairs in water. *Wear*, 263(7-12):920–929, 2007.

[25] M Varenberg, G Halperin, and I Etsion. Different aspects of the role of wear debris in fretting wear. *Wear*, 252(11-12):902–910, 2002.

[26] U Pettersson and S Jacobson. Friction and wear properties of micro textured dlc coated surfaces in boundary lubricated sliding. *Tribology letters*, 17(3):553–559, 2004.

[27] A Blatter, M Maillat, SM Pimenov, GA Shafeev, AV Simakin, and EN Loubnin. Lubricated sliding performance of laser-patterned sapphire. *Wear*, 232(2):226–230, 1999.

[28] YP Chiu. An analysis and prediction of lubricant film starvation in rolling contact systems. *ASLE transactions*, 17(1):22–35, 1974.

[29] I Demirci, S Mezghani, M Yousfi, H Zahouani, and M El Mansori. The scale effect of roughness on hydrodynamic contact friction. *Tribology Transactions*, 55(5):705–712, 2012.

[30] I Křupka, M Vrbka, and M Hartl. Effect of surface texturing on mixed lubricated non-conformal contacts. *Tribology International*, 41(11):1063–1073, 2008.

[31] C Greiner, M Schafer, U Popp, and P Gumbsch. Contact splitting and the effect of dimple depth on static friction of textured surfaces. *ACS applied materials & interfaces*, 6(11):7986–7990, 2014.

[32] S C Vladescu, A V Olver, I G Pegg, and T Reddyhoff. The effects of surface texture in reciprocating contacts–an experimental study. *Tribology International*, 82:28–42, 2015.

[33] S C Vlădescu, A Ciniero, K Tufail, A Gangopadhyay, and T Reddyhoff. Looking into a laser textured piston ring-liner contact. *Tribology International*, 115:140–153, 2017.

[34] S C Vlădescu, S Medina, A V Olver, I G Pegg, and T Reddyhoff. The transient friction response of a laser-textured, reciprocating contact to the entrainment of individual pockets. *Tribology Letters*, 62(2):19, 2016.

[35] S C Vlădescu, S Medina, A V Olver, I G Pegg, and T Reddyhoff. Lubricant film thickness and friction force measurements in a laser surface textured reciprocating line contact simulating the piston ring–liner pairing. *Tribology International*, 98:317–329, 2016.

[36] S C Vlădescu, A V Olver, I G Pegg, and T Reddyhoff. Combined friction and wear reduction in a reciprocating contact through laser surface texturing. *Wear*, 358:51–61, 2016.

[37] S C Vlădescu, A Ciniero, K Tufail, A Gangopadhyay, and T Reddyhoff. Optimization of pocket geometry for friction reduction in piston–liner contacts. *Tribology Transactions*, 61(3):522–531, 2018.

[38] Doris Nekesa Khaemba, Abdullah Azam, TianLong See, Anne Neville, and Farnaz Motamen Salehi. Understanding the role of surface textures in improving the performance of boundary additives, part i: Experimental. *Tribology International*, page 106243, 2020.

[39] Philipp G Grützmacher, Francisco J Profito, and Andreas Rosenkranz. Multi-scale surface texturing in tribologycurrent knowledge and future perspectives. *Lubricants*, 7(11):95, 2019.

[40] A Azam, A Ghanbarzadeh, A Neville, A Morina, and M CT Wilson. Modelling tribochemistry in the mixed lubrication regime. *Tribology International*, 132:265–274, 2019.

[41] A Azam, A Dorgham, P Parsaeian, A Morina, A Neville, and MCT Wilson. The mutual interaction between tribochemistry and lubrication: Interfacial mechanics of tribofilm. *Tribology International*, 2019.

[42] A Azam, A Dorgham, A Morina, A Neville, and MCT Wilson. A simple deterministic plastoelastohydrodynamic lubrication (pehl) model in mixed lubrication. *Tribology International*, 131:520–529, 2019.

[43] Abdullah Azam. *Modelling interfacial tribochemistry in the mixed lubrication regime*. PhD thesis, University of Leeds, 2018.

[44] Abdel Dorgham, Pourya Parsaeian, Abdullah Azam, Chun Wang, Ardian Morina, and Anne Neville. Single-asperity study of the reaction kinetics of p-based triboreactive films. *Tribology International*, 133:288–296, 2019.

[45] Abdel Dorgham, Abdullah Azam, Ardian Morina, and Anne Neville. On the transient decomposition and reaction kinetics of zinc dialkyldithiophosphate. *ACS applied materials & interfaces*, 10(51):44803–44814, 2018.

[46] X Ai. Numerical analyses of elastohydrodynamically lubricated line and point contacts with rough surfaces by using semi-system and multigrid methods (volumes 1 and 2). 1993.

[47] Y-Z Hu and D Zhu. A full numerical solution to the mixed lubrication in point contacts. *Journal of Tribology*, 122(1):1–9, 2000.

[48] Ramsey Gohar. *Elastohydrodynamics*. World Scientific, 2001.

[49] S Liu, Q Wang, and G Liu. A versatile method of discrete convolution and fft (dc-fft) for contact analyses. *Wear*, 243(1-2):101–111, 2000.

[50] WZ Wang, H Wang, YC Liu, YZ Hu, and D Zhu. A comparative study of the methods for calculation of surface elastic deformation. *Proceedings of the Institution of Mechanical Engineers, Part J: Journal of Engineering Tribology*, 217(2):145–154, 2003.

[51] Izhak Etsion. Improving tribological performance of mechanical components by laser surface texturing. *Tribology letters*, 17(4):733–737, 2004.

[52] HL Costa and Ian Michael Hutchings. Some innovative surface texturing techniques for tribological purposes. *Proceedings of the Institution of Mechanical Engineers, Part J: Journal of Engineering Tribology*, 229(4):429–448, 2015.

	symbol	value	units
Applied load	F	50	N
Radius of curvature (pin)	R_1	10	mm
Radius of curvature (plate)	R_2	∞	mm
Surface speed (pin)	U_1	0.0	mm/s
Surface speed (plate)	U_2	20.0	mm/s
Young's modulus (pin)	E_1	134	GPa
Young's modulus (plate)	E_2	206	GPa
Poisson ratio (pin)	ν_1	0.26	$----$
Poisson ratio (plate)	ν_2	0.29	$----$
Roughness (pin)	Sq_1	0.046	μm
Roughness (plate)	Sq_2	0.007	μm
Kinematic viscosity	η	19.3	$c.St.$
Density of oil	ρ	0.8	g/cm^3
Pressure-viscosity coefficient	α	11 $\times 10^{-9}$	Pa^{-1}

Table 1: Input values

Surface texture	Skewness (S_{sk})	Direction (S_{td})	Aspect ratio (S_{tr})
T1	-0.371	90^o	0.835
T2	-0.821	60^o	0.619
T3	-0.718	90^o	0.016
Non-textured	0.441	133^o	0.034

Table 2: Texture geometrical parameters

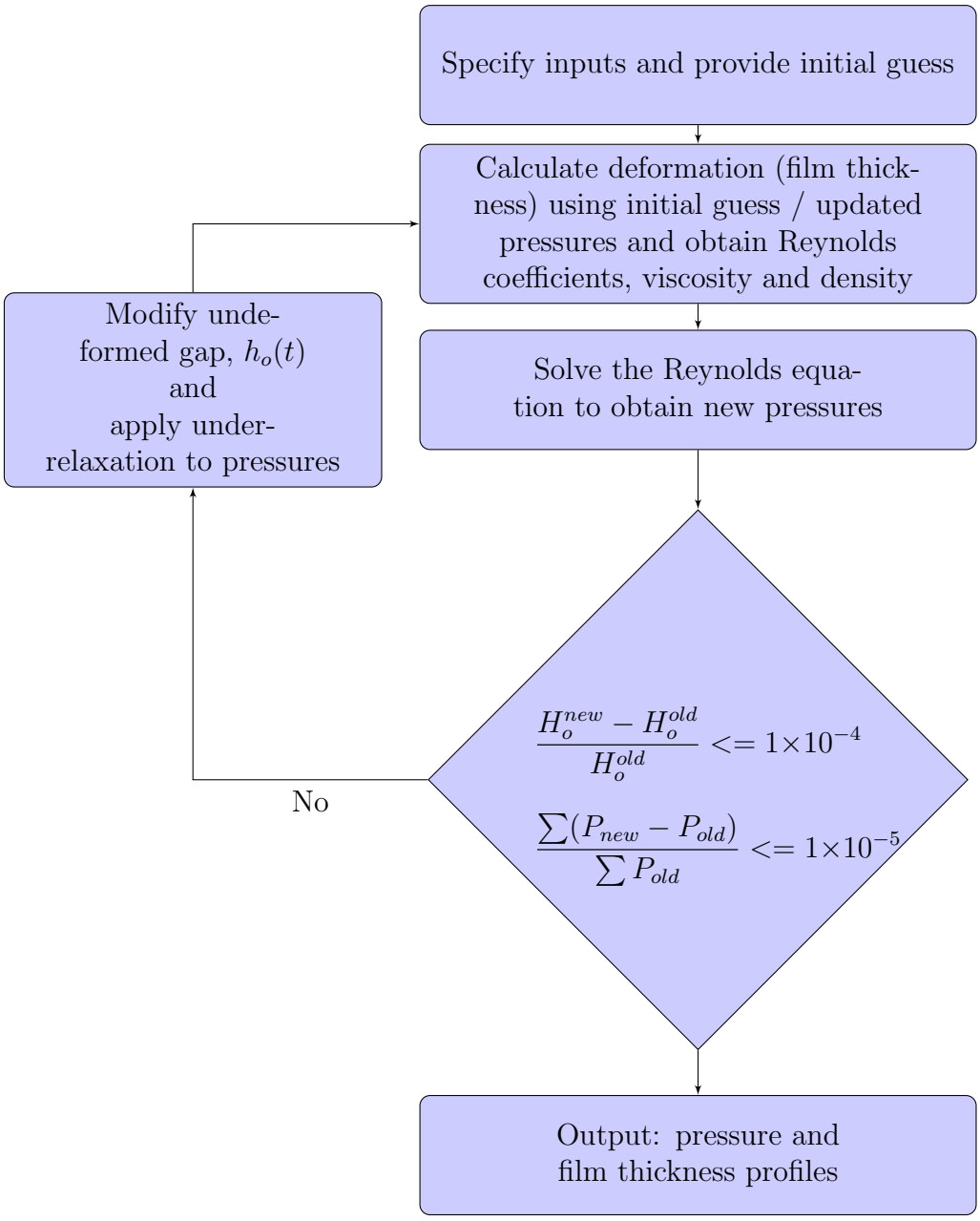

Figure 1: The numerical algorithm to solve the mixed lubrication equations

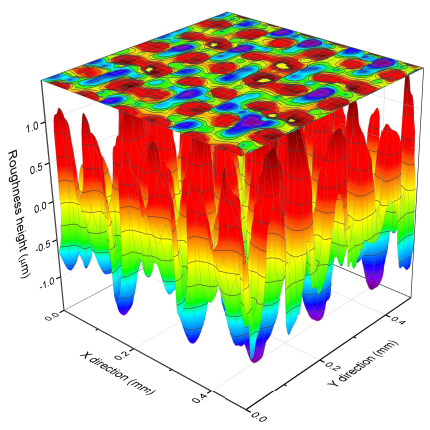

(a) Texture, T1

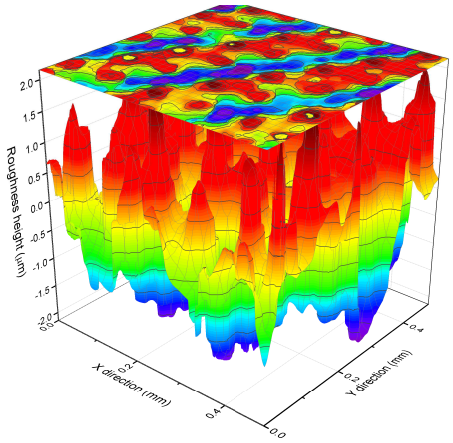

(b) Texture, T2

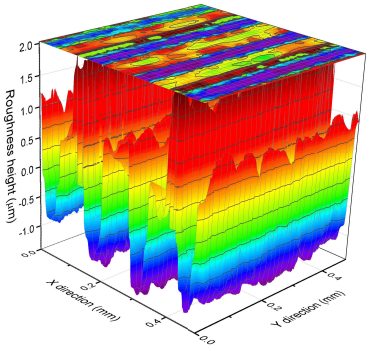

(c) Texture, T3

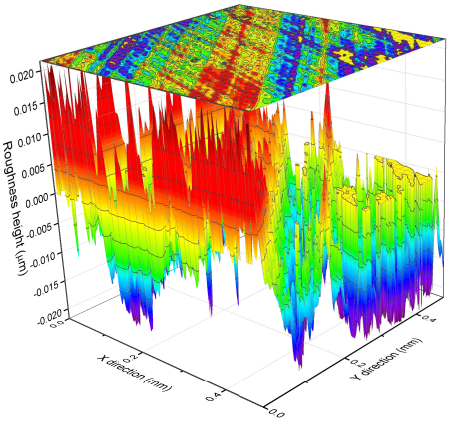

(d) Polished

Figure 2: Illustrations of the imported textures on a 256×256 grid. The X-direction represents the direction of flow.

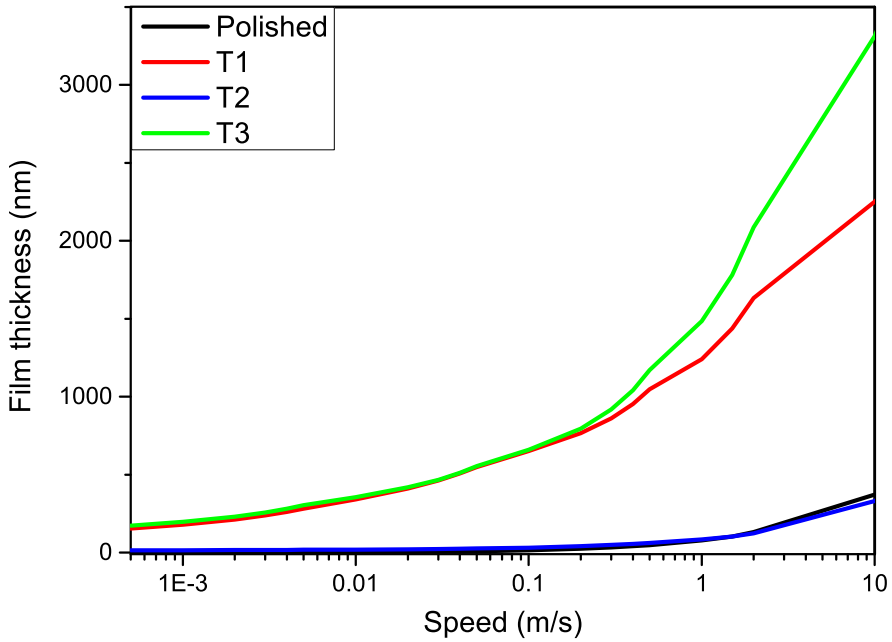

Figure 3: The variation of average film thickness with sliding speed for different textured surfaces.

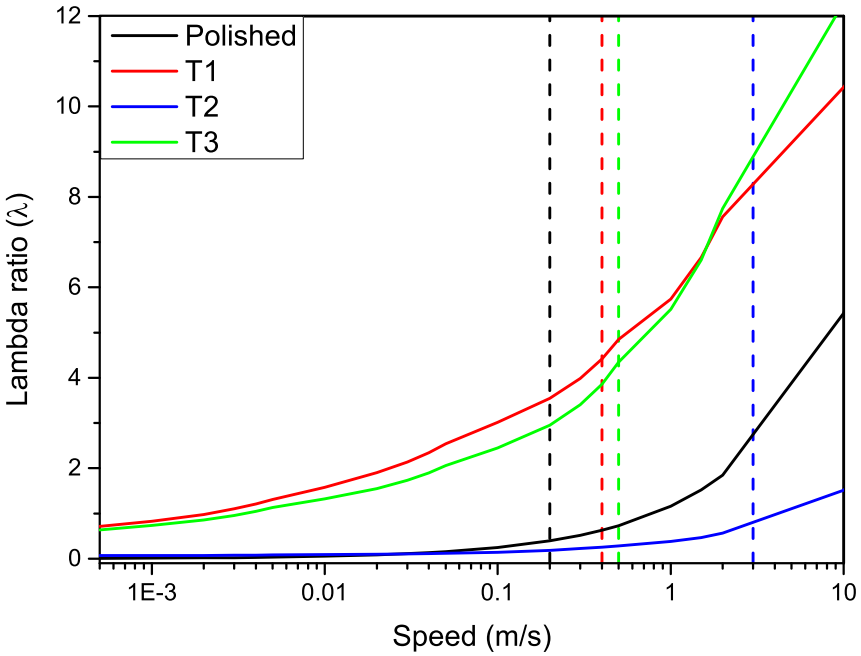

Figure 4: The variation of lambda ratio with sliding speed for different textured surfaces. The dashed lines correspond to the lubrication transition from EHL to mixed for corresponding textures.

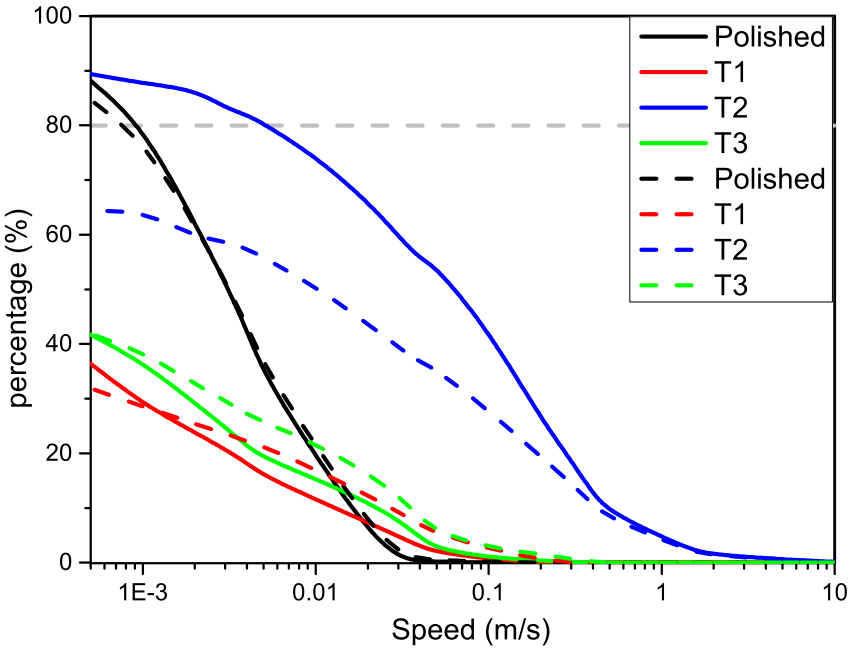

Figure 5: The contact load ratio, W_c (solid lines) and contact area ratio, A_c (dashed lines) as a function of sliding speed for different textured surfaces. Grey dashed line at $80\%W_c$ represents the full boundary lubrication condition

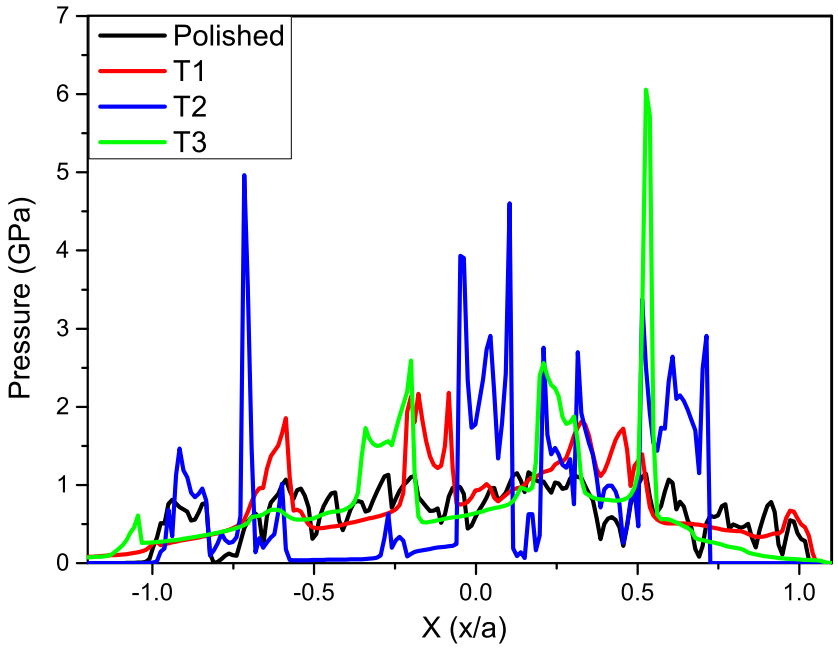

Figure 6: A comparison of pressures generated within the contact with different textured surfaces at speed of 0.02 m/s

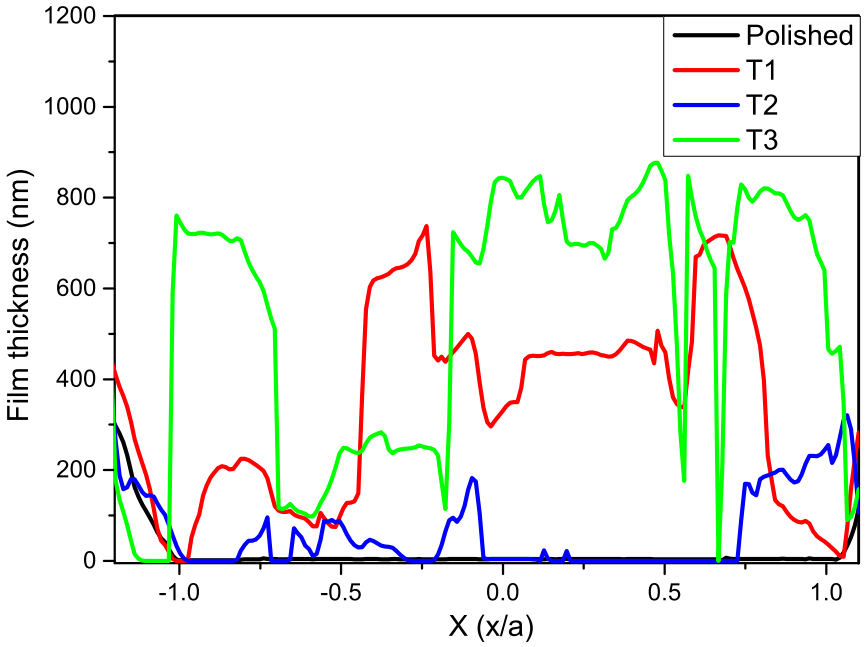

Figure 7: A comparison of lubricant film thickness values generated within the contact with different textured surfaces at speed of 0.02 m/s